J Mater Sci: Mater Electron (2023) 34:1188

Rietveld refined structural, dielectric, and impedance properties of lead-free $1-x(K_{0.4}Na_{0.6}Nb_{0.96}Sb_{0.04}O_3)$-$x(Bi_{0.5}K_{0.5}TiO_3)$ ($0.00 \leq x \leq 0.07$) composites

Madan Lal[1,2,*], Priyanka Thakur[2], Prashant Thakur[2], Navdeep Sharma[3], Pankaj Sharma[4], and Anoop Kumar Shukla[5]

[1] *School of Physics and Materials Science, Shoolini University, Solan, HP 173229, India*
[2] *Department of Physics, ACBS, Eternal University, Baru Sahib, Sirmaur, HP 173101, India*
[3] *Department of Physics, School of Basic Sciences, Abhilashi University, Mandi, HP 175028, India*
[4] *Applied Science Department, National Institute of Technical Teachers Training and Research, Chandigarh 160019, India*
[5] *Department of Physics, Amity Institute of Applied Sciences, Amity University, Noida, UP 201313, India*

Received: 18 March 2023
Accepted: 4 May 2023

ABSTRACT

A lead-free series of $1-x(K_{0.4}Na_{0.6}Nb_{0.96}Sb_{0.04}O_3)$-$x(Bi_{0.5}\ K_{0.5}TiO_3)$ ($0.00 \leq x \leq 0.07$) composites were prepared by the conventional solid-state reaction route. Rietveld's refined XRD pattern revealed phase transitions from orthorhombic (Amm2) to rhombohedral (R3m) and rhombohedral to tetragonal (P4mm) with $x = 0.03$ and 0.05 content of $(Bi_{0.5}K_{0.5}TiO_3)$. SEM images reveal that the microstructure consists of small, randomly oriented, well-inter-linked, and non-uniform-shaped grains. Dielectric study indicates that Curie temperature (T_C) decreases from 340 to 160 °C as the BKT content increases from $x = 0.00$ to 0.07 and the first transition temperature shifts below room temperature. The complex modulus plots exhibited two semicircles, confirming the ceramics' presence of bulk grain and grain boundary. The impedance and modulus plots confirm the presence of a non-Debye type of relaxation in the ceramics. The ac conductivity increases with a rise in the temperature, confirming negative temperature coefficient resistance (NTCR) behavior. Therefore, conductivity may increase due to the charge carrier hopping rate or the oxygen vacancies (V''_O).

1 Introduction

Pb-based perovskite materials have been widely used in electronic devices (like sensors, buzzers, transducers, actuators, etc.), because of their exceptional features like high Curie temperature (T_C), and high thermal stability. However, Pb-based materials have lots of demerits: toxic, harmful effects on human health, causing cancer, thermal decomposition during synthesis and processing, and even challenging to dispose [1–6]. Thus, researchers have made several efforts to develop lead-free perovskite materials with

---

Address correspondence to E-mail: madan.physics26@gmail.com

https://doi.org/10.1007/s10854-023-10580-x

comparable properties to Pb-based ceramics in the last few years. In this regard, several lead-free materials have been reported, such as $BaTiO_3$ (BT), $BiFeO_3$, $Bi_{0.5}K_{0.5}TiO_3$ (BKT), $K_{0.5}Na_{0.5}NbO_3$ (KNN), $Bi_{0.5}Na_{0.5}TiO_3$ (BNT), $LiNaNbO_3$ (LNN), and their composites like KNN-BKT, KNN-LT, KNN-LS, BT-BF, BT-LNN [7–12], etc.

In these days, KNN-based materials are promoted as a research hot spot because it has (i) possible ions substitutions, (ii) high piezoelectric coefficient ($d_{33} \sim 700$ pC/N) [13], (iii) high Curie temperature ($T_C \sim 420$ °C), (iv) superior piezoelectric properties [14], and (v) especially, several phase transitions with temperature rise (i.e., rhombohedral–orthorhombic (*R–O*), orthorhombic–tetragonal (*O–T*), and tetragonal–cubic (*T–C*) at 123, 200, and 410 °C, respectively) [15, 16]. In 2004, Saito [7] reported the *O–T* phase boundary was obtained near room temperature by doping $Li^{+}/Ta^{5+}/Sb^{5+}$ ions in KNN ceramics. Likui et al. [17] reported in a report that Sb-doping promotes the formation of a pure single crystalline $(K_{0.7}Na_{0.3})(Nb_{0.95}Sb_{0.05})$ phase without the excess existence of Na and K ions. Sb^{5+}-doping also affects the surface morphology by increasing the spontaneous polarization, thus improving the electric properties of KNN ceramics. Later, Wu et al. [18] were also able to explore and understand the effect of various dopants on the shifting of phase boundaries and construction of new phase boundary. Sb^{5+} dopant also helps to densify the phase zone in KNN ceramics [1].

Bismuth potassium titanate (BKT) is a well-known lead-free ferroelectric perovskite ceramic with a high T_C of 380 °C and good dielectric properties compared to other single piezoelectric ceramics. BKT also shows two anomalies peaks in temperature-dependent dielectrics like KNN and BT. The first transition in BKT takes place from tetragonal to pseudo-cubic phase at ~ 290 °C and finally transfer to cubic phase (T_C) at 380 °C [19–21]. Therefore, BKT is appropriate for developing lead-free materials for wide-range temperature applications. Many potential applications such as aerospace, automobiles, geological exploration, and so on [22, 23] need high-temperature devices ($T_C > 300$ °C); for such applications, piezoelectric ceramics with high T_C are important [24]. Therefore, new lead-free composites of KNNS and BKT perovskite materials were chosen for this work to obtain improved structural and dielectric properties. In the present work, synthesis and investigation of structural, dielectric, and impedance properties of the new composition of $1-x(K_{0.5}Na_{0.5}Nb_{0.96}Sb_{0.04}O_3)$-$x(Bi_{0.5}K_{0.5}TiO_3)$ (abbreviated as KNNS-BKT) composites were done.

2 Materials and methods

The powders of K_2CO_3, Na_2CO_3, Nb_2O_5 Sb_2O_3, Bi_2O_3, and TiO_2 were weighted accordingly to the stoichiometric with x = 0.00, 0.01, 0.03, 0.05, and 0.07). The composite of $1-x(K_{0.4}Na_{0.6}Nb_{0.96}Sb_{0.04}O_3)$-$x(Bi_{0.5}K_{0.5}TiO_3)$ was synthesized in two steps. First, the precursor of $(K_{0.4}Na_{0.6})(Nb_{0.96}Sb_{0.04})O_3$ and $(Bi_{0.5}K_{0.5})TiO_3$ was simultaneously blended using an agate mortar and pestle in an ethanol media for 6–8 h. Then these two powders were calcined at an optimized temperature of 900 and 1050 °C for 5 h. The proposed chemical reaction for the formations of KNNS and BKT is given in Eqs. (1) and (2), respectively (symbol ↓ indicates the addition of $0.02(O_2)$, into the mixture as mixing is done in the open-air environment during the evaporation of ethanol. The symbol ↑ represents the burnout gases during the calcination). Finally, these powders were grinded to get fine powders with no agglomerations.

$$0.2(K_2CO_3) + 0.3(Na_2CO_3) + 0.48(Nb_2O_5) + 0.02(Sb_2O_3) + 0.02(O_2) \downarrow \xrightarrow{\text{calcinedat900°C}} K_{0.4}Na_{0.6}Nb_{0.96}Sb_{0.04}O_3 + \tfrac{1}{2}\,CO_2 \uparrow \quad (1)$$

$$0.25(Bi_2O_3) + 0.25(K_2CO_3) + TiO_2 \xrightarrow{\text{calcinedat1050°C}} Bi_{0.5}K_{0.5}TiO_3 + \tfrac{1}{4}\,CO_2 \uparrow \quad (2)$$

In the 2nd step, these fine precursors of powders were combined under the stoichiometric with $x = 0.00$, 0.01, 0.03, 0.05, and 0.07 to obtain powders of $1-x(K_{0.4}Na_{0.6}Nb_{0.96}Sb_{0.04}O_3)$-$x(Bi_{0.5}K_{0.5}TiO_3)$ using a 10% molar solution of PVA (polyvinyl alcohol) as the binder. This mixture was cold pressed into disk-shaped pallets of 10 mm diameter and 2 mm thickness with the help of a hydraulic press (pressure of 60 MPa). Thereafter, these green pallets were sintered at 1100 °C for 4 h. The phase and purity of these ceramics were done through the X-ray diffraction technique with Cu Kα ($\lambda = 1.5406$ Å) in the 2θ range of 20° to 60° at room temperature. surface morphology of these composites was tested via scanning electron microscopy (SEM, JEOL 7600F). The dielectric and impedance properties of these sintered ceramics were tested using the Impedance Analyzer (HIOKI IM 3570) in 1 kHz–10 MHz frequency range with a temperature range of 25 to 400 °C after double-side silver paste.

3 Results and discussion

Figure 1a shows the XRD pattern of $1-x(K_{0.4}Na_{0.6}Nb_{0.96}Sb_{0.04}O_3)$-$x(Bi_{0.5}K_{0.5}TiO_3)$, $0.00 \le x \le 0.07$ composites in the 2θ range from 20° to 60°. The XRD spectra of KNNS-BKT composites exhibit well-defined diffraction peaks at 2θ of 22.46°, 31.88°, 45.85°, 51.60°, and 56.96° suggesting the rhombohedral structure (with space group = *A*mm2) [25]. A magnified XRD pattern in the 2θ range of 44.5° to 47° is shown in Fig. 1b to clarify the peak shape differences further. The expanded XRD pattern shows the peaks shifting toward a higher angle. These peaks shift may be attributed due to the replacement of relatively smaller cation Ti^{4+}(∼ 0.61 Å) for Nb^{+5} (∼ 0.69 Å) at the B-site in ABO_3, which results in the lattice compression with an increase in BKT content [26–28].

Rietveld refinement (using *Fullprof software*) of the XRD pattern of $1-x(K_{0.4}Na_{0.6}Nb_{0.96}Sb_{0.04}O_3)$-$x(Bi_{0.5}K_{0.5}TiO_3)$, $0.00 \le x \le 0.07$ composites was carried out further to confirm the crystal structure and lattice parameters shown in Fig. 2a–e. Refinement reveals that $x \le 0.01$ is characteristic of the orthorhombic (O) phase (with space group = Amm2) [29, 30] that was found in these composites, which means a minute amount of BKT cannot change the crystal structure. As x was increased to 0.03, indicating the coexistence of orthorhombic (O) and rhombohedral (R) phases with Amm2, and R3m space group. At $x = 0.05$, the phase $T_{O\text{-}R}$ turns to the rhombohedral–tetragonal ($T_{R\text{-}T}$) phase (in Fig. 2(d)), and finally, in Fig. 2(e) at $x = 0.07$ the crystal structure results in the

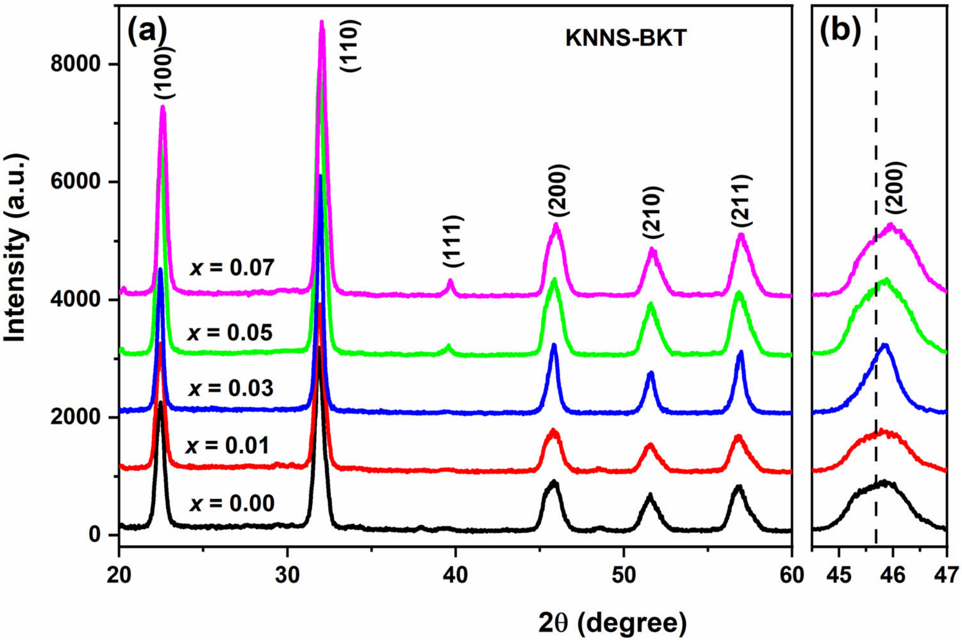

Fig. 1 X-ray diffractometer patterns of $1-x(K_{0.4}Na_{0.6}Nb_{0.96}Sb_{0.04}O_3)$-$x(Bi_{0.5}K_{0.5}TiO_3)$, $0.00 \le x \le 0.07$ composites: **a** $2\theta = 20°–60°$, **b** $2\theta = 44^0—47.^0$

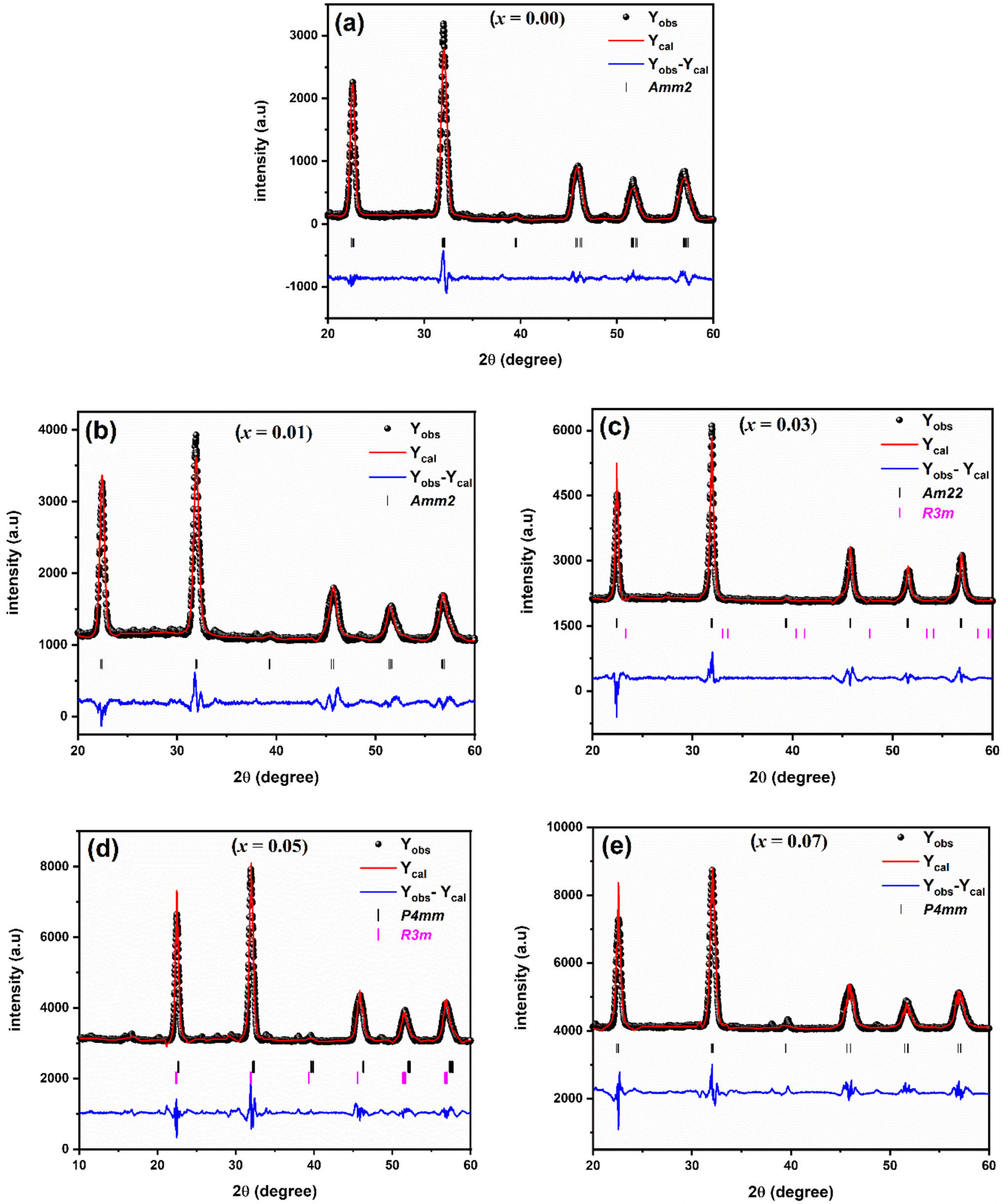

Fig. 2 Rietveld refinement of XRD patterns of $1-x(K_{0.4}Na_{0.6}Nb_{0.96}Sb_{0.04}O_3)$-$x(Bi_{0.5}K_{0.5}TiO_3)$, $0.00 \le x \le 0.07$ composites

Table 1 Rietveld refined lattice and crystallographic parameters of $1-x(K_{0.4}Na_{0.6}Nb_{0.96}Sb_{0.04}O_3)$-$x(Bi_{0.5}K_{0.5}TiO_3)$, $0.00 \le x \le 0.07$ composites

Simulated/calculated crystallographic parameters	$x = 0.00$	$x = 0.01$	$x = 0.03$		$x = 0.05$		$x = 0.07$
Lattice parameters							
a (Å)	5.625 (1)	3.980 (9)	3.960 (5)	5.340 (4)	5.532 (4)	3.954 (7)	3.940 (1)
b (Å)	5.649 (8)	5.610 (2)	5.613 (6)	5.340 (4)	5.532 (4)	3.954 (7)	3.940 (1)
c (Å)	5.596 (8)	5.592 (2)	5.600 (6)	6.700 (9)	6.819 (2)	3.978 (6)	3.972 (4)
(Space group)	(Amm2)			(R3m)		(P4mm)	
Phase fraction (%age)	100		99.25	0.75	1.71	98.29	100
R-factors							
R_{bragg}	4.01	3.27	3.39	48.8	6.94	2.35	3.12
R_f	2.13	1.50	1.33	48.8	8.10	1.76	2.19
R_p	14.8	21.7	1.18	26.0	1.18	21.0	24.4
R_{wp}	15.3	15.2	2.12	16.6	1.85	13.3	15.1
R_{exp}	9.49	13.7	2.11	16.48	1.73	12.41	13.9
GOF (χ^2)	2.60	1.33	1.01		1.14		1.18
Volume per unit cell (Å^3)	187.99 (2)	124.85(8)	124.45 (2)	166 (3)	180.72 (3)	62.19 (1)	61.67 (7)
Crystallite Size (nm)	27.2	27.5	39		33.8		33.3

formation of a tetragonal structure with an increase in BKT content [31]. Therefore, this investigation confirms that stable solutions are formed between KNNS and BKT. Rietveld's refined lattice parameters are listed in Table 1. The value of χ^2 and R_{wp} is in the range of 2.60–1.01 and 1.85–16.60, respectively, indicating the high reliability of refined parameters of KNNS-BKT composite ceramics [32–34].

Figure 3a–e represents the microstructure of $1-x(K_{0.4}Na_{0.6}Nb_{0.96}Sb_{0.04}O_3)$-$x(Bi_{0.5}K_{0.5}TiO_3)$, $0.00 \le x \le 0.07$ composites and were recorded at 1 µm resolution. The SEM images consist of randomly oriented, well-inter linked non-uniform (shape and size) grains. A slight decrease in average grain size was measured in the range of 2.88 to 0.52 µm. It is obvious that with the increase of BKT content, the pores in the samples also increase gradually (as clearly shown in Fig. 2(c, e)). This can be explained by taking into account the lower relative mobility of the dopant ions ($Bi^{3+}$and Ti^{4+}) in contrast to host ions during the sintering process, which inhibits grain development [31, 35–37]. Thus, an increase in porosity leads to a decrease in grain size, and inhomogeneous distribution of the grains may be due to the presence of different cations at the A and B sites in these perovskite composites. This increase in pores may be the reason for the inclination to spread and finally take on a flat shape of dielectric peaks [38–40]. The value of the average grains of the respective samples is given in Table 2.

Temperature-dependent dielectric spectra anticipate the evidence for confirming phase structure and phase transitions in ceramics [39, 41, 42]. Figure 4a–e shows the recorded dielectric constant (ε) of $1-x(K_{0.4}Na_{0.6}Nb_{0.96}Sb_{0.04}O_3)$-$x(Bi_{0.5}K_{0.5}TiO_3)$, $0.00 \le x \le 0.07$ composites in the temperature range of $20° \le T \le 400$ °C at different frequencies (i.e., 1 kHz, 10 kHz, 100 kHz, and 1 MHz, respectively). For the composites with $x \le 0.03$ (as shown in Fig. 4(a–c)), two dielectric anomaly peaks with temperature rise from 20 to 400 °C were observed, corresponding O–T ($T_{O–T}$) and T–C (T_C) phase transitions, respectively. The O–T dielectric peak near the low temperature exhibits frequency dispersion characteristics due to the thermal evolution of polar nanoregions (PNRs) formed by strong polarity phases R3m and Amm2, respectively. $T_{O\text{-}R}$ gradually moves toward the low temperature as BKT content increases. For $x = 0.00$, the dielectric peak is larger than that of the other four samples. It is well known that dielectric behavior comes from the bulk of the materials (i.e., grain of larger size with homogeneity). It can be seen in the SEM image that KNNS has a larger grain size with homogeneity which may be responsible for the larger dielectric peak for $x = 0.00$. While the addition of BKT into the KNNS crystal lattice causes the composition disorder, which makes

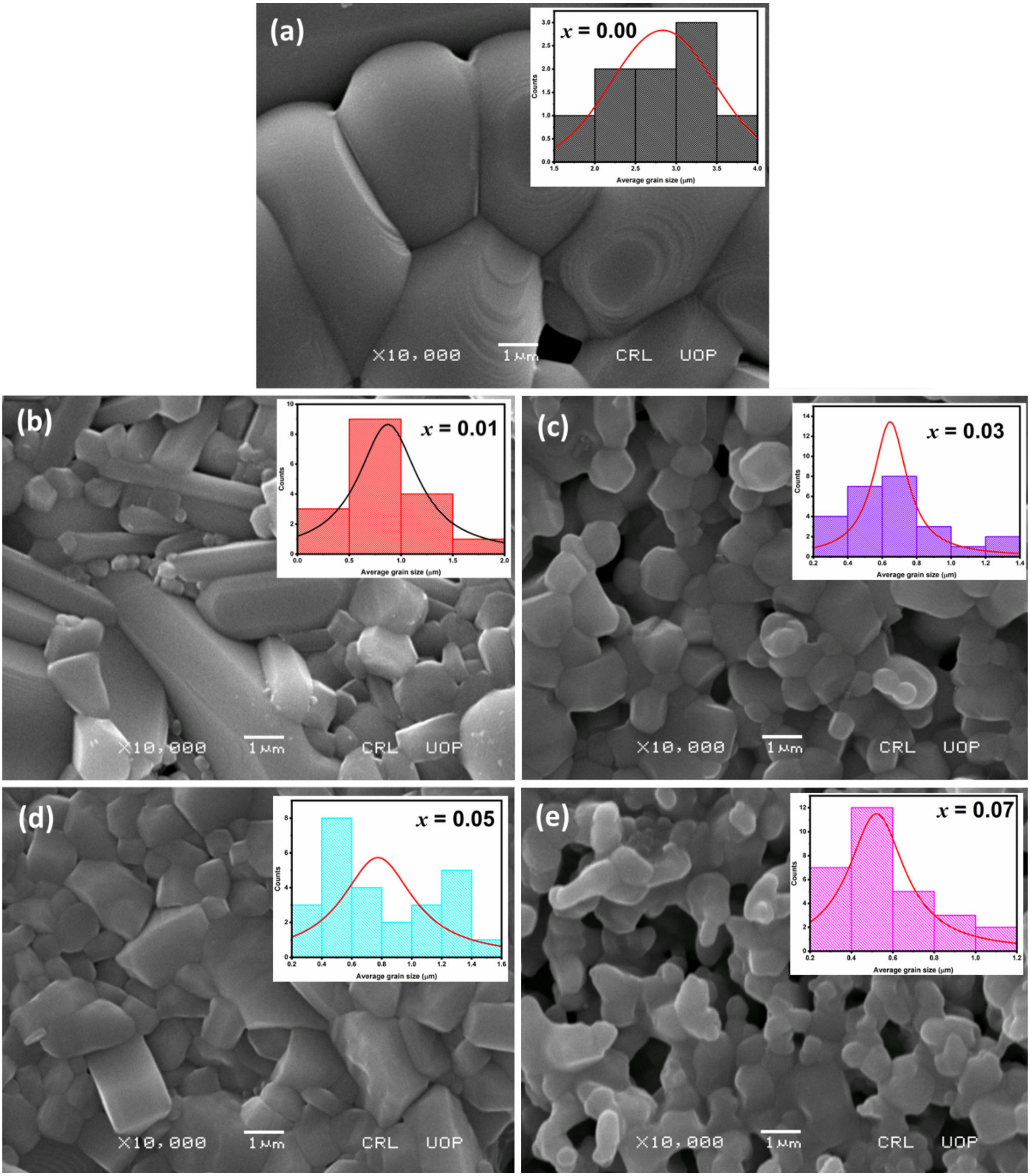

Fig. 3 SEM images for $1-x(K_{0.4}Na_{0.6}Nb_{0.96}Sb_{0.04}O_3)$-$x(Bi_{0.5}K_{0.5}TiO_3)$, $0.00 \leq x \leq 0.07$ composites

the composites more favorable for nanodomain wall motion and nanodomain switching. T_C is associated with the phase transitions of PNRs from R3m and Amm2 to the P4mm phase. Generally, a relaxor phase transition from non-ergodic to ergodic occurs during the temperature swaps from T_1 to T_C [43, 44]. As the amount of BKT increases, the $T_{O\text{-}T}$, $T_{R\text{-}T}$, and T_C simultaneously shift toward the lower temperature.

Table 2 Physical parameters of $1-x(K_{0.4}Na_{0.6}Nb_{0.96}Sb_{0.04}O_3)$-$x(Bi_{0.5}K_{0.5}TiO_3)$, $0.00 \leq x \leq 0.07$ composites

Composition	Frequency (k Hz)	T_1 °C	T_{max} °C	ε_{max}	Diffusivity (γ)	Average grain size (µm)
$x = 0.00$	1	50	340	9159	0.64	2.88
	10	50	340	8383	0.98	
	100	50	340	7882	1.18	
$x = 0.01$	1	50	330	5010	1.13	0.89
	10	50	330	4643	1.26	
	100	50	330	4448	1.37	
$x = 0.03$	1	57	290	5961	1.19	0.65
	10	57	290	5417	1.36	
	100	57	290	5180	1.49	
$x = 0.05$	1	–	160	1930	0.16	0.78
	10	–	210	1704	0.31	
	100	–	230	1493	0.33	
$x = 0.07$	1	–	80	7156	1.30	0.52
	10	–	80	3488	1.08	
	100	–	90	2355	0.53	

Whereas for $x = 0.05$ in Fig. 4(d), the inhomogeneous nature of grain distribution may be the reason for the low dielectric peak. Also for $x = 0.05$ and 0.07 composites, the 1st transition peaks shifted to below room temperature (which was out of the instrumental range), there is one only dielectric peak at T_C. All these results are consistent with XRD as well as with the Rietveld refinements [30, 45–47]. Therefore, an increase in x leads to a shift of the T_C toward the room temperature in all compositions, and the first phase transition transferred below the room temperature to $x = 0.05$ and 0.07. The dielectric constant (ε_{max}) values and Curie temperature (T_C) of respective samples at different frequencies are listed in Table 2.

The degree of diffuse phase transition is determined by applying the Currie–Weiss law fitting to the dielectric data; $\gamma = 1$ for normal ferroelectric and $\gamma = 2$ for the relaxor behavior. If γ lies in between 1 and 2, indicating the diffused ferroelectric characteristic of the materials. The modified Currie–Weiss law given in Eq. (3) was used to calculate γ:

$$\left(\frac{1}{\varepsilon} - \frac{1}{\varepsilon_{max}}\right) = (T - T_{max})^{\gamma} \quad (3)$$

where ε_{max} = maximum dielectric constant at the phase transition temperature T_{max}, and γ is the degree of diffuseness. From Fig. 5a–e, it was observed that the diffusivity factor value (γ) increases from 0.64 to 1.30 as BKT content is increased from 0.00 to 0.07, respectively. The increase in the value of γ can correspond to the compositional fluctuations that result in the broadening of peaks in the dielectric spectra. The lowest value of diffusion coefficient for $x = 0.05$ (in Fig. 5(d)) may be due to the coexistence of rhombohedral and tetragonal structure at this value of x. Because of the coexistence of the crystal structure, the crystallites liquefy at different temperatures and hence, can't diffuse properly. Thus, getting a low diffusion coefficient (γ) particularly at $x = 0.05$. While at $x = 0.07$ in Fig. 5(e), crystallites have a single crystal structure because of which crystal liquefies at almost the same temperature and leads to an increase in the diffusion coefficient. The various values of γ are listed in Table 2.

Complex impedance spectroscopy (CIS) is a powerful technique that helps to explore the various conduction mechanisms, relaxation processes, and dielectric vacancies in ceramics. Cole–cole plots usually have three semicircles corresponding to grain, grain boundary, and grain-electrode effects for polycrystalline materials. These semicircles are usually seen to be due to the trapping of oxygen vacancies and other defects. They are also used to calculate the capacitance and resistance value of the respective grain and grain boundary effect.

Figure 6a–e shows the fitted Nyquist plots of $1-x(K_{0.4}Na_{0.6}Nb_{0.96}Sb_{0.04}O_3)$-$x(Bi_{0.5}K_{0.5}TiO_3)$, $0.00 \leq x \leq 0.07$ composites at temperatures of 340, 370, and 400 °C, respectively. All the composites exhibit only one depressed semicircular arc with

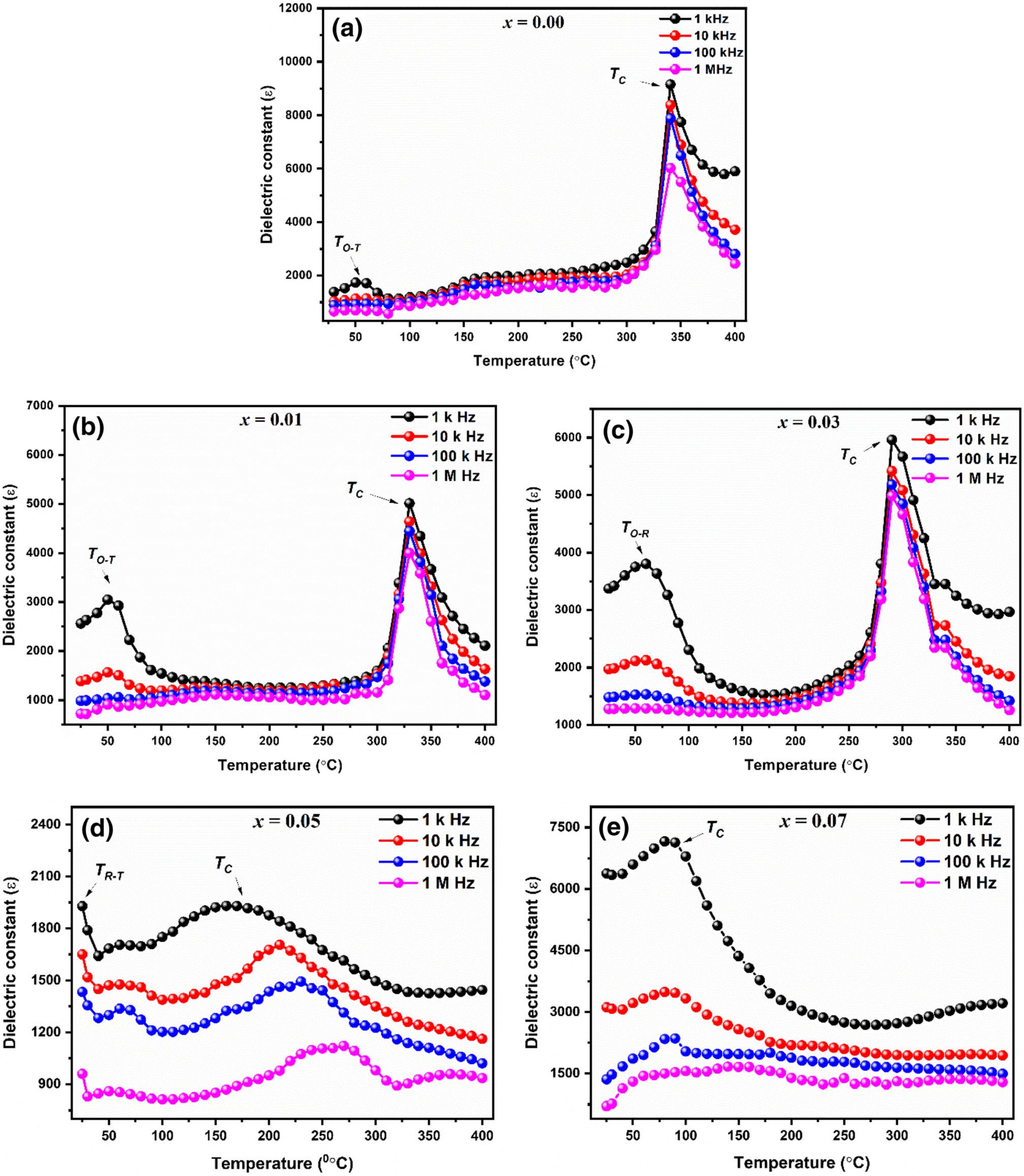

Fig. 4 Variation of dielectric constant (ε) with temperature $1-x(K_{0.4}Na_{0.6}Nb_{0.96}Sb_{0.04}O_3)$-$x(Bi_{0.5}K_{0.5}TiO_3)$, $0.00 \le x \le 0.07$ composites at different frequencies

centers below the real axis at higher temperatures. Further, the arc radii decrease with a temperature rise, suggesting (i) the NTCR (Negative Temperature Coefficient of Resistance) behavior of these composites and (ii) the mobility of space charge becomes easier at higher temperatures, often found in

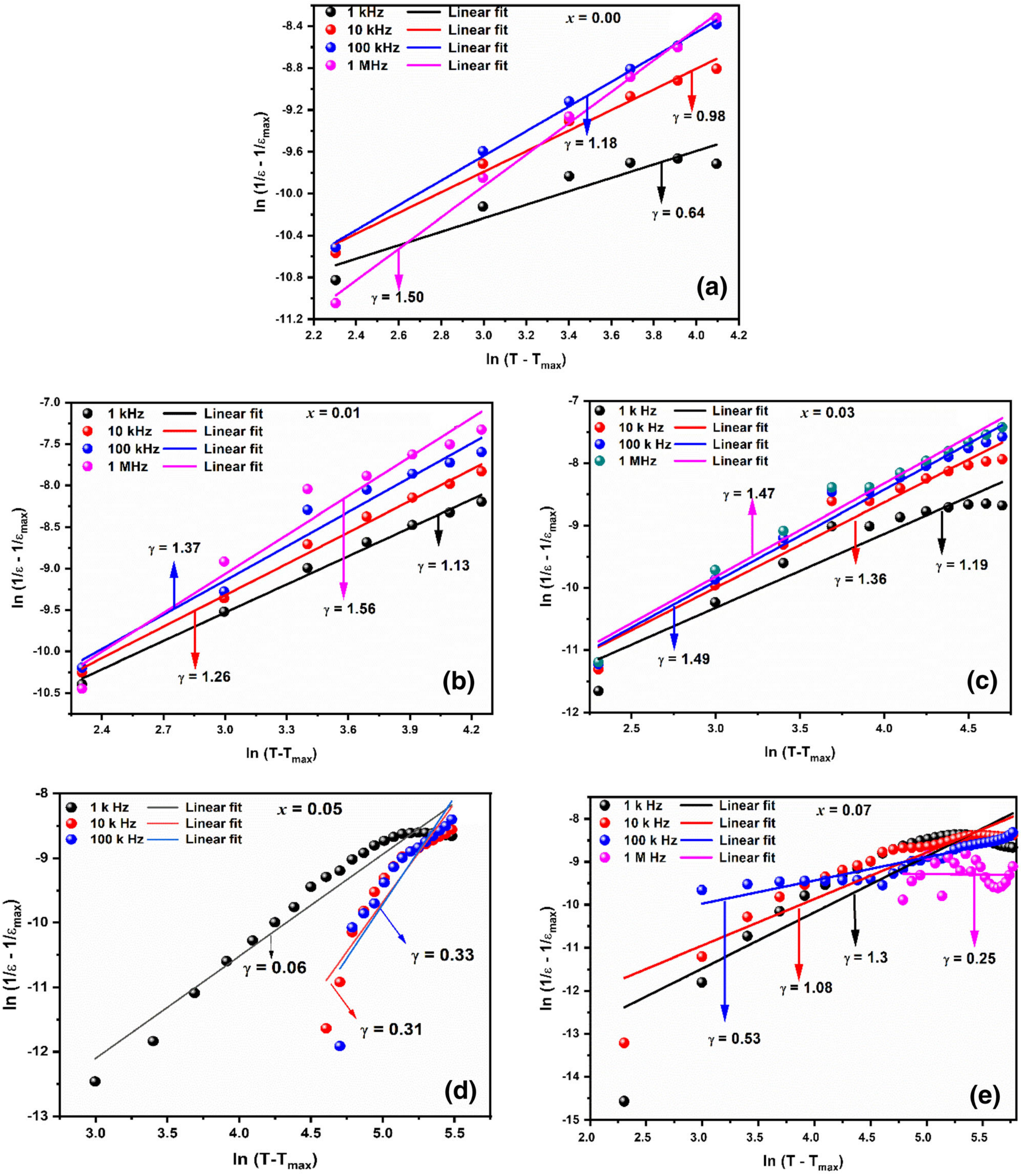

Fig. 5 Variation of ln $(1/\varepsilon - 1/\varepsilon_{max})$ as a function of ln $(T\text{–}T_{max})$ of $1{-}x(K_{0.4}Na_{0.6}Nb_{0.96}Sb_{0.04}O_3)$-$x(Bi_{0.5}K_{0.5}TiO_3)$, $0.00 \le x \le 0.07$ composites at different frequencies

semiconductors. This further suggests these composites' non-Debye-type relaxation processes [48]. In general, the formation of these semicircular arcs depends upon the relaxation strength and the applied frequency range (i.e., instrumental frequency range). *Z-Simp Win software* was used to fit the

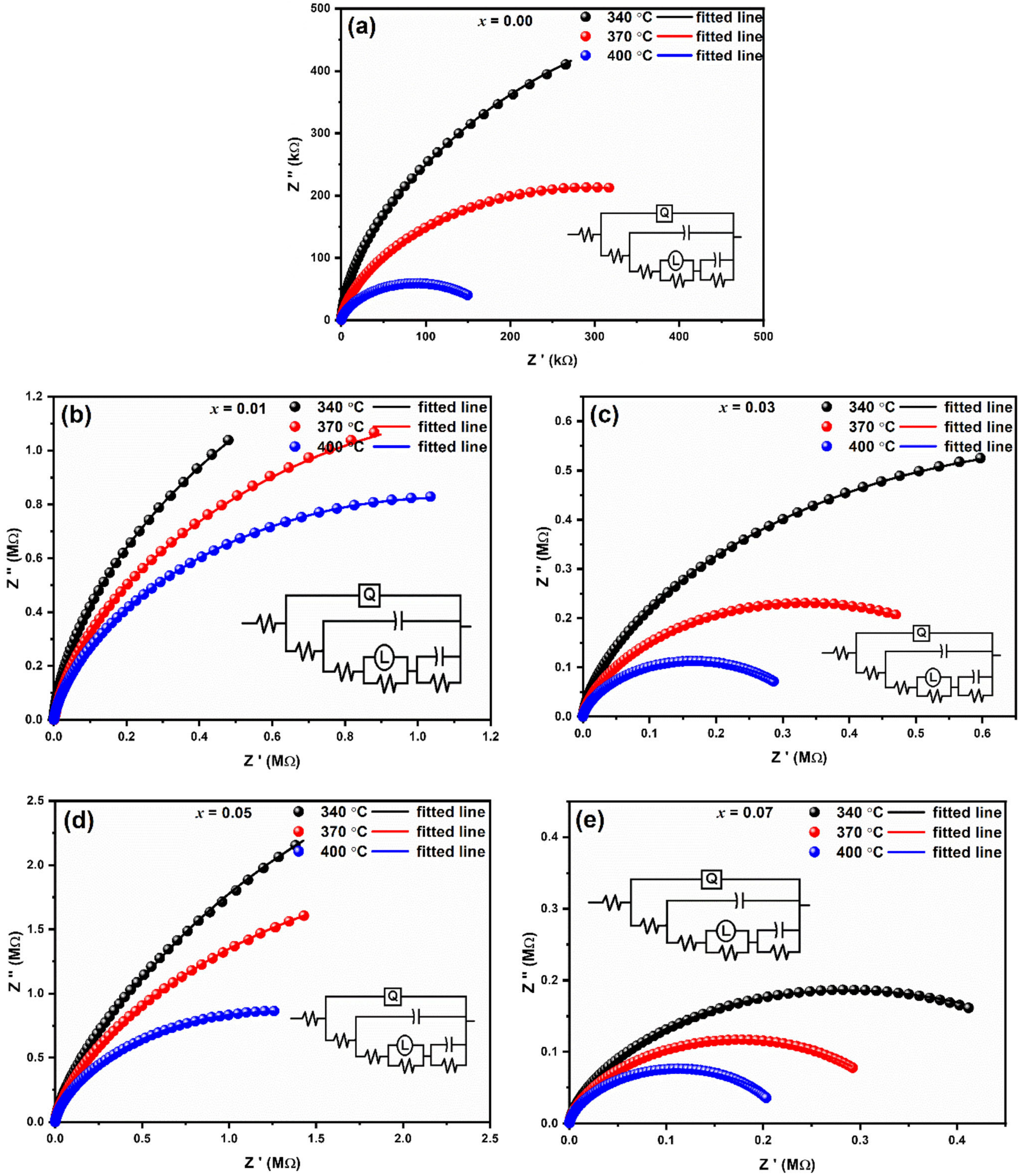

Fig. 6 Variation of the real (Z') and imaginary (Z'') part of impedance at selected temperatures of $1-x(K_{0.4}Na_{0.6}Nb_{0.96}Sb_{0.04}O_3)$-$x(Bi_{0.5}K_{0.5}TiO_3)$, $0.00 \leq x \leq 0.07$ composites modeled impedance spectrum using the calculated values of circuit elements and for fitted values

Table 3 Parameters calculated from impedance fitted data $1-x(K_{0.4}Na_{0.6}Nb_{0.96}Sb_{0.04}O_3)$-$x(Bi_{0.5}K_{0.5}TiO_3)$, $0.00 \le x \le 0.07$ composites

Compositions	Temperature (°C)	Resistance		n	Q	Activation energy (E_a)	
		R_g (Ωcm^2)	R_{gb} (Ωcm^2)			1 kHz	10 kHz
$x = 0.00$	340	2.562×10^{1}	7.265×10^{2}	9.667×10^{-1}	2.591×10^{-9}	0.30	0.16
	370	2.197×10^{1}	1.021×10^{7}	5.863×10^{-1}	2.560×10^{-8}		
	400	9.155×10^{0}	1.000×10^{7}	5.950×10^{-1}	3.821×10^{-8}		
$x = 0.01$	340	5.863×10^{5}	1.572×10^{-1}	6.501×10^{-1}	4.408×10^{-9}	1.11	1.10
	370	6.470×10^{2}	1.840×10^{-1}	9.280×10^{-1}	1.245×10^{-9}		
	400	5.016×10^{3}	1.000×10^{-2}	6.907×10^{-1}	3.828×10^{-9}		
$x = 0.03$	340	9.342×10^{0}	1.087×10^{-1}	5.473×10^{-1}	1.879×10^{-8}	0.25	0.19
	370	1.551×10^{-1}	1.108×10^{1}	5.771×10^{-1}	1.673×10^{-8}		
	400	1.000×10^{-7}	9.361×10^{-2}	6.016×10^{-1}	1.688×10^{-8}		
$x = 0.05$	340	1.696×10^{2}	1.339×10^{6}	9.501×10^{-1}	4.783×10^{-10}	1.5	1.0
	370	0.690×10^{2}	1.639×10^{6}	9.501×10^{-1}	4.983×10^{-10}		
	400	8.029×10^{1}	1.006×10^{1}	5.736×10^{-1}	7.883×10^{-9}		
$x = 0.07$	340	1.113×10^{2}	2.670×10^{5}	9.081×10^{-1}	1.325×10^{-9}	1.7	1.2
	370	2.853×10^{1}	2.073×10^{1}	6.079×10^{-1}	1.779×10^{-8}		
	400	1.000×10^{-1}	1.988×10^{9}	8.621×10^{-1}	2.327×10^{-9}		

experimental data. In Fig. 6a–e, the experimental data and fit are represented by symbols (●) and (▬) in black, red, and blue color, respectively. An attempt has been made to clear the ins and outs of the system (with an equivalent circuit), which is helping to establish a relationship between the electrical and structural properties of these composites. A constant phase element has been used to recompense the non-Debye response, in addition to capacitors and resistors. The circuit-related parameters are listed in Table 3.

Figure 7a–e includes the variation of the Z'' with the frequency for $1-x(K_{0.4}Na_{0.6}Nb_{0.96}Sb_{0.04}O_3)$-$x(Bi_{0.5}K_{0.5}TiO_3)$, $0.00 \le x \le 0.07$ composites. Z'' (f) plots show two distinct regimes within the measured frequency range: (i) a dispersion region and (ii) a plateau region. In the dispersion region, a monotonic decrease in the magnitude of Z'' (at different higher temperatures) was observed in the low-frequency region. The frequency where all peaks merge is called fusion frequency ($\sim$ 10 kHz). The merging phenomena of Z'''s magnitude at fusion frequency indicate the accumulation of space charges and provide evidence for the homogeneous nature of the samples under the applied external field. Interestingly, a decrease in the Z'''s magnitude was observed with the temperature rise, supporting the NTCR behavior of ceramics. There is a peak observed for $x = 0.07$ in Fig. 7(e), which may be due to (i) the high doping concentration of BKT in the KNNS crystal lattice, and (ii) the high concentration of Bi and Ti-ions in the ceramics may cause the number of dielectric relaxations.

Complex modulus spectroscopy is a major tool to inspect the dynamic aspects of electrical transport phenomena: hopping mechanism, electrical transport of carriers/ions, conductivity relaxation time, etc., which are overlapped and unidentifiable due to different relaxation times.

The complex modulus spectra of M'' versus M' for $1-x(K_{0.4}Na_{0.6}Nb_{0.96}Sb_{0.04}O_3)$-$x(Bi_{0.5}K_{0.5}TiO_3)$, $0.00 \le x \le 0.07$ composites are represented in Fig. 8a–e. Two semicircle arcs with their center below the real axis confirm the non-Debye type relaxations in these composites. First semicircle at a lower frequency is due to grain, and the second one is due to grain boundary capacitance being responsible for the conduction mechanism at higher temperatures (which is not visible in the Nyquist plots (i.e., Figure 6)).

Figure 9a–e represents the variation of the imaginary part of the electric modulus (M'') with frequency at higher temperatures of $1-x(K_{0.4}Na_{0.6}Nb_{0.96}Sb_{0.04}O_3)$-$x(Bi_{0.5}K_{0.5}TiO_3)$, $0.00 \le x \le 0.07$ composites. A peak between 0.1 and 1000 k Hz for $x = 0.01$ is observed, but the magnitude of the peak is very small. This may be due to the low value of BKT content (which means BKT content does not get the appropriate space in the KNNS crystal lattice). But

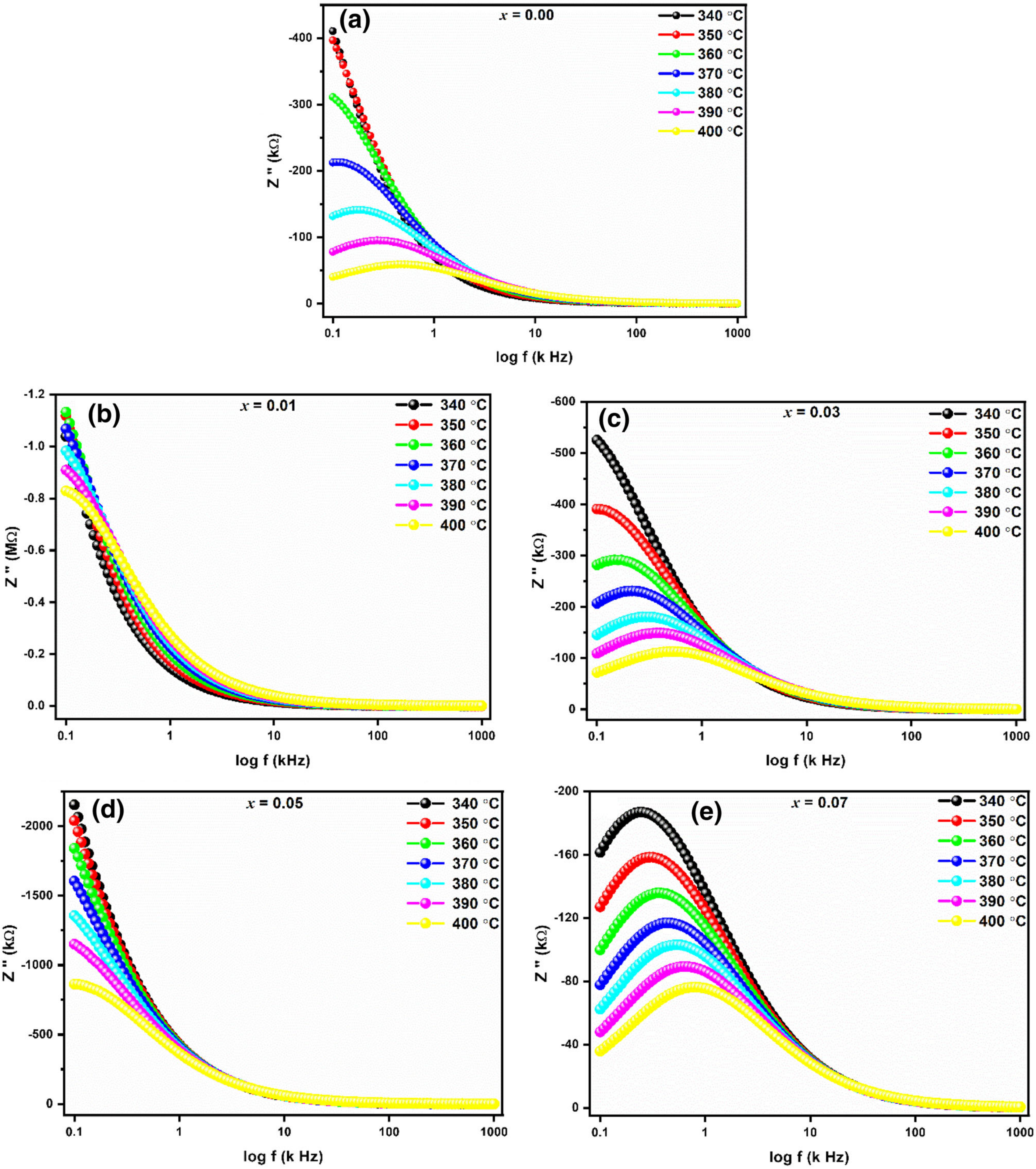

Fig. 7 Variation of imaginary part of impedance (Z'') with frequency of $1-x(K_{0.4}Na_{0.6}Nb_{0.96}Sb_{0.04}O_3)$-$x(Bi_{0.5}K_{0.5}TiO_3)$, $0.00 \leq x \leq 0.07$ composites at different temperatures

for a higher value of BKT content, BKT properly takes the position in the crystal lattice of KNNS. Therefore, clear and broadened peaks were formed, as the BKT content increased. The broadened and asymmetric peaks indicate the non-Debye relaxation. A shift in the (M''_{max}) peak to higher frequencies with a rise in the temperature may be due to the correlated motion of mobile ions. At frequency above peak maximum,

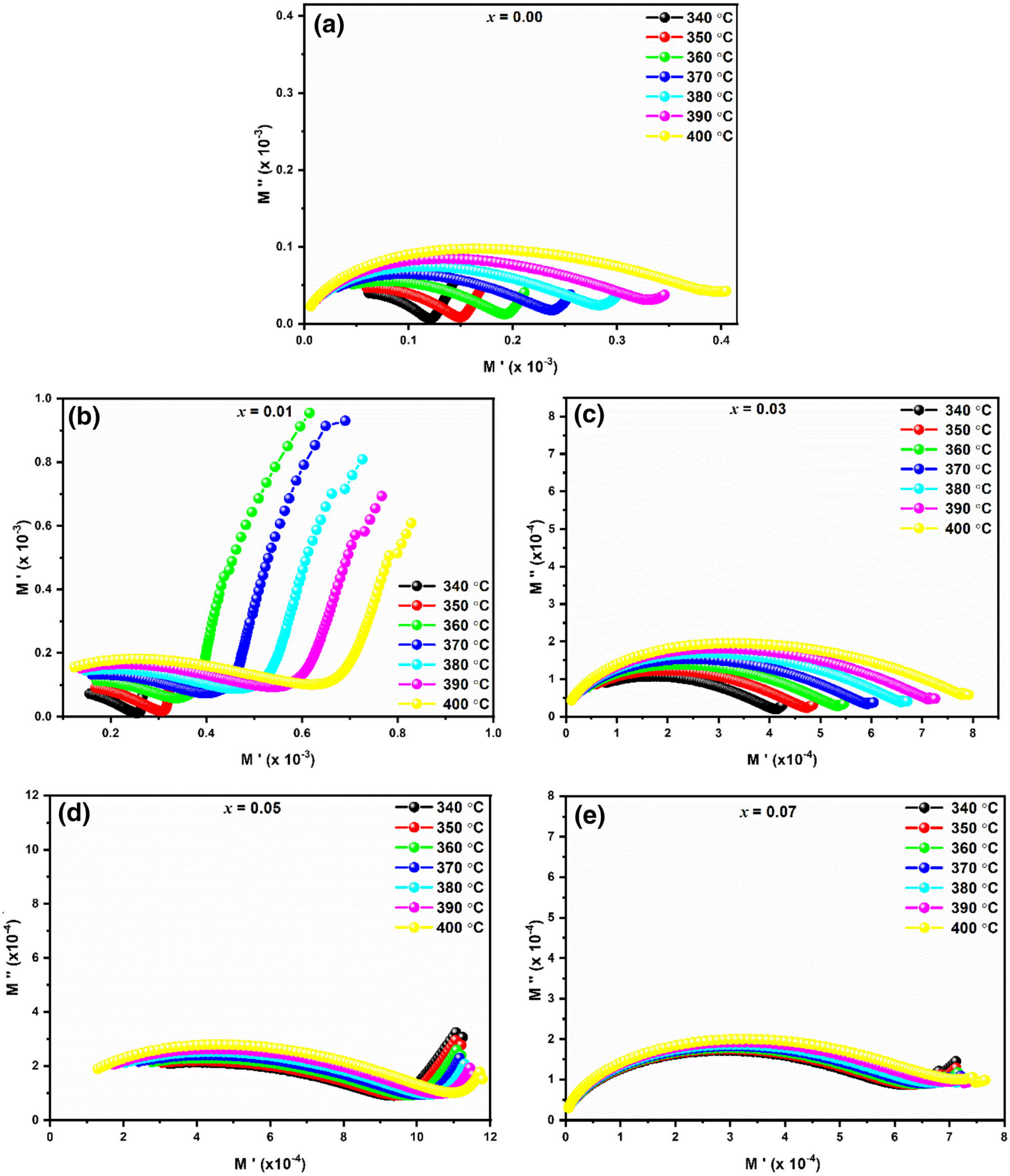

Fig. 8 Variation of real part of modulus (M') with imaginary part of modulus (M'') of $1-x(K_{0.4}Na_{0.6}Nb_{0.96}Sb_{0.04}O_3)$-$x(Bi_{0.5}K_{0.5}TiO_3)$, $0.00 \leq x \leq 0.07$ composites at different selected temperatures

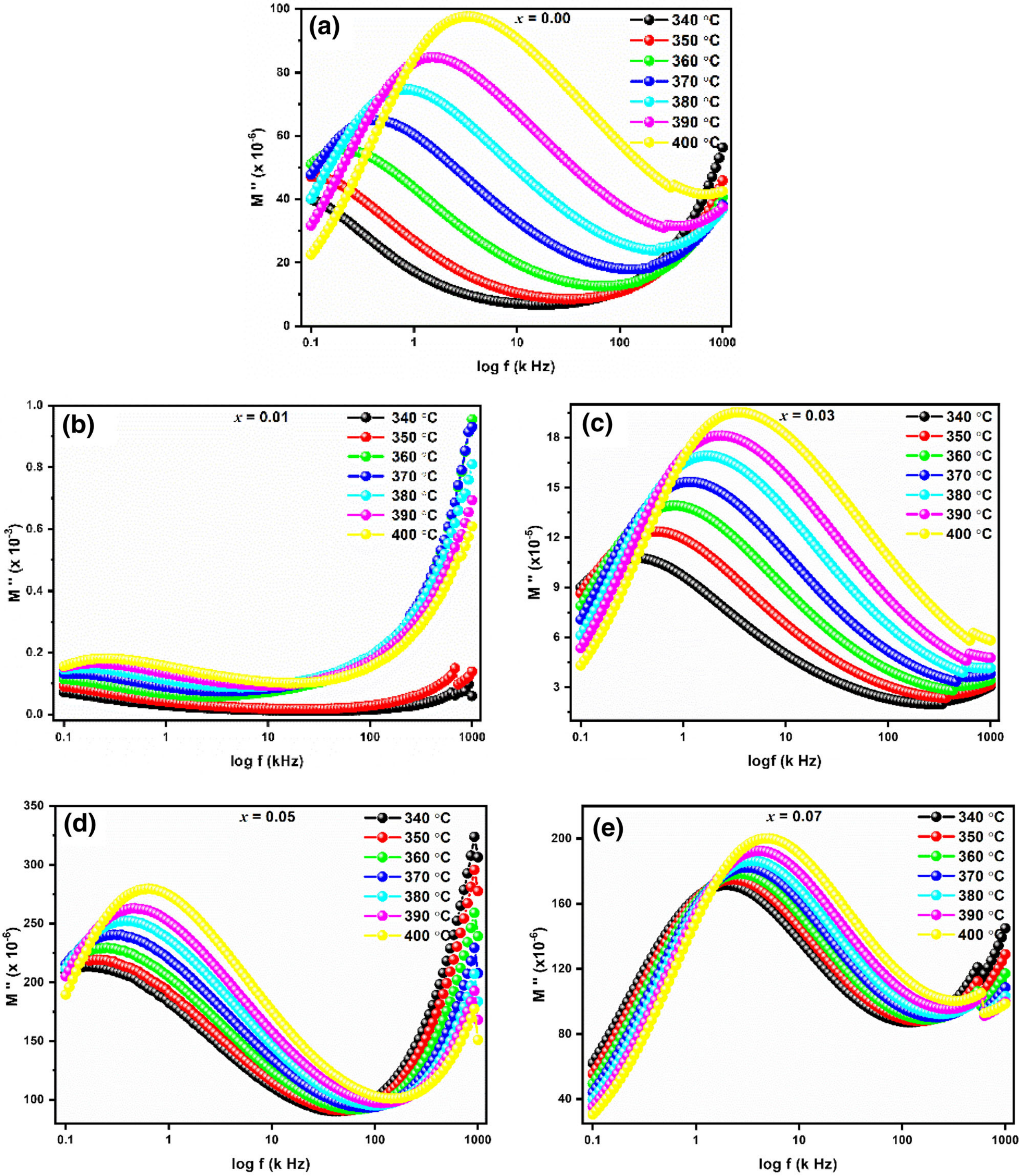

Fig. 9 Variation of imaginary part of modulus (M'') with frequency of $1-x(K_{0.4}Na_{0.6}Nb_{0.96}Sb_{0.04}O_3)$-$x(Bi_{0.5}K_{0.5}TiO_3)$, $0.00 \le x \le 0.07$ composites at different temperatures

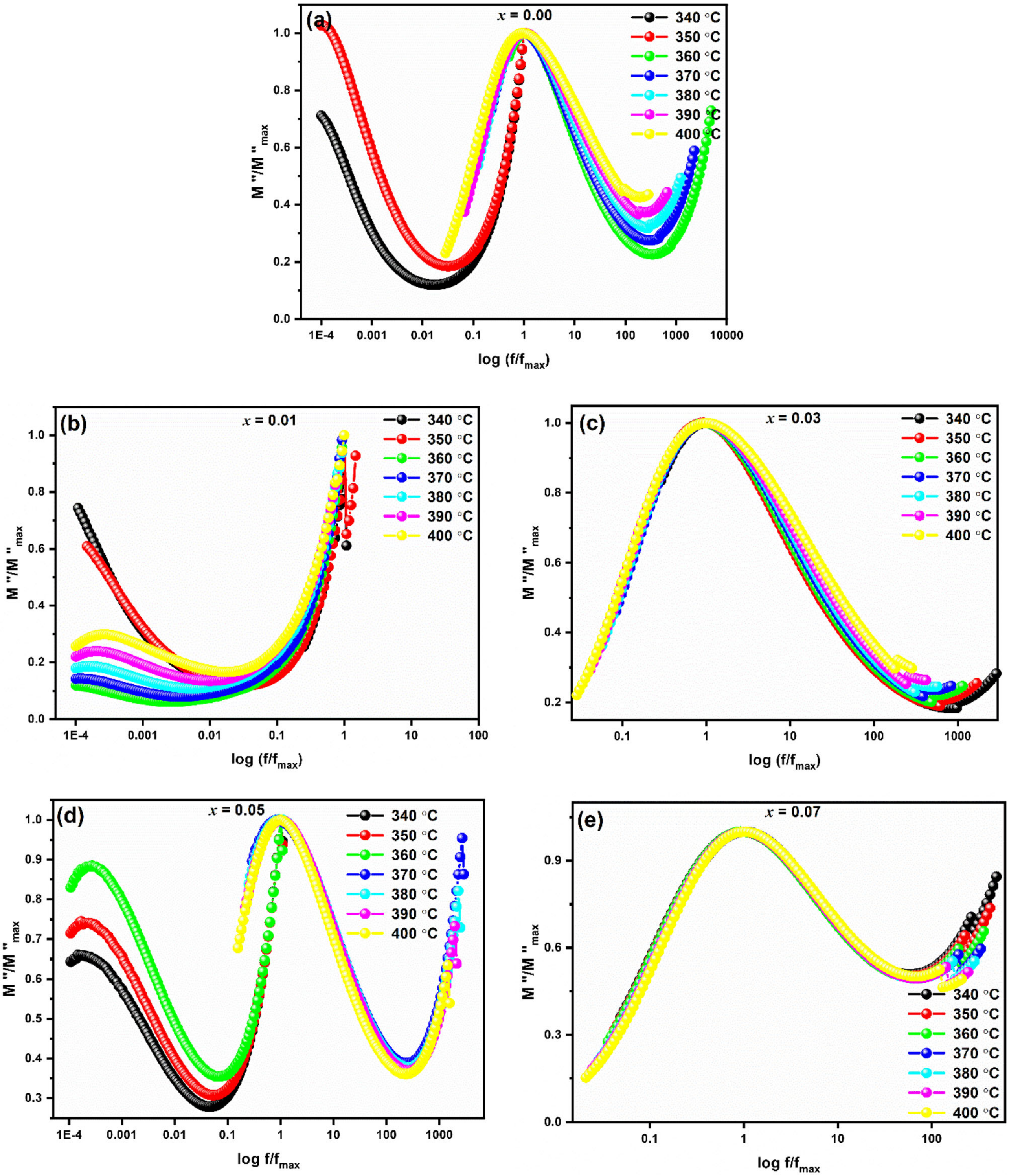

Fig. 10 Impedance scaling behavior of (Z''/Z''_{max}) vs log (f/f_{max}) of $1-x(K_{0.4}Na_{0.6}Nb_{0.96}Sb_{0.04}O_3)$-$x(Bi_{0.5}K_{0.5}TiO_3)$, $0.00 \leq x \leq 0.07$ composites at different temperatures

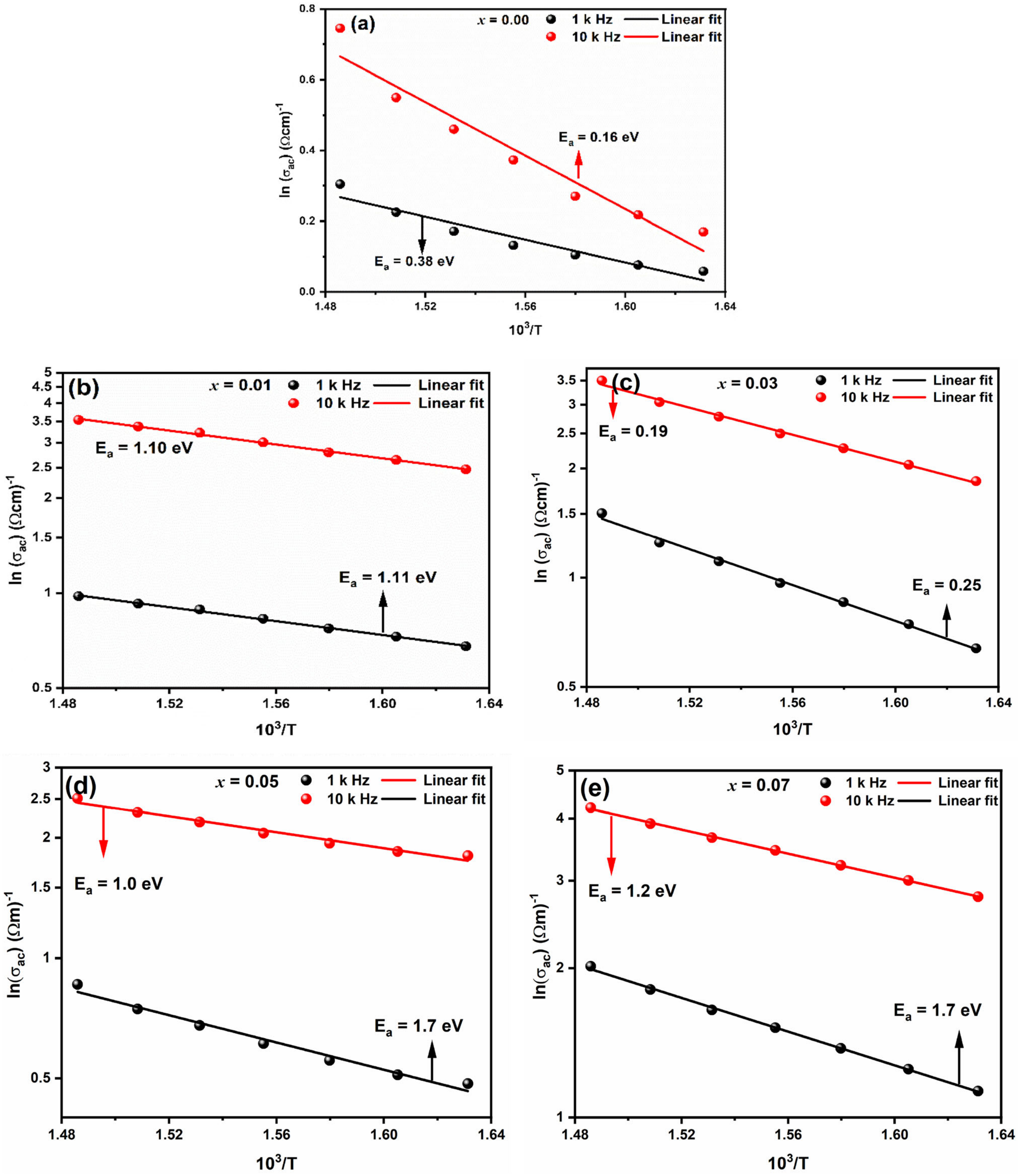

Fig. 11 Variation of ac electrical conductivity (σ_{ac}) as a function of the reciprocal temperature of $1-x(K_{0.4}Na_{0.6}Nb_{0.96}Sb_{0.04}O_3)$-$x(Bi_{0.5}K_{0.5}TiO_3)$, $0.00 \le x \le 0.07$ composites at frequencies 1 k Hz and 10 k Hz

the carriers are confined to potential wells, being mobile for short distances. The frequency at which $M''_{\max}$ is obtained is called relaxation frequency. The frequency below the $M''_{\max}$ helps in determining the mobility range of charge carriers for long distances [49].

Figure 10a–e represents the variation of the $M''/M''_{\max}$ versus log $(f/f_{\max})$ at different temperatures for the $1-x(K_{0.4}Na_{0.6}Nb_{0.96}Sb_{0.04}O_3)$-$x(Bi_{0.5}K_{0.5}TiO_3)$, $0.00 \le x \le 0.07$ composites. The normalized spectra reveal all the peaks overlapped on a single master curve at different temperatures, indicating that the relaxation behavior is temperature-independent. Furthermore, the full width at half-maxima (FWHM) was calculated and is about 1.211, also confirming the time-independent relaxation distribution and thus indicating the non-Debye relaxation [50].

Figure 11a–e shows the variation of $\ln\sigma_{ac}$ with reciprocal temperature $(10^3/T)$ for $1-x(K_{0.4}Na_{0.6}Nb_{0.96}Sb_{0.04}O_3)$-$x(Bi_{0.5}K_{0.5}TiO_3)$, $0.00 \le x \le 0.07$ composites at selected frequencies (i.e. , 1 kHz and 10 kHz). The activation energy for conductivity ion was obtained by fitting the experimental data with the Arrhenius relationship:

$$\sigma_{ac} = \sigma_0 \exp\left(-E_a/K_B T\right) \tag{4}$$

$$\ln \sigma_{ac} = \ln\left(\sigma_0\right)\left(-E_a/K_B T\right) \tag{5}$$

where σ_{ac} is ac conductivity, σ_0 = pre-exponential factor, (K_B 1.38 × 10^{-23} JK^{-1}) is Boltzmann constant, E_a = activation energy, and T is the absolute temperature.

In this present study, the observed ac conductivity of the composites increases from (0.28×10^{-5} to 2.0×10^{-5}) $(\Omega m)^{-1}$ and (0.68×10^{-5} to 4.3×10^{-5}) $(\Omega m)^{-1}$ as the BKT content increased at frequencies 1 and 10 kHz, respectively. The increase in ac conductivity with a temperature rise confirms the NTCR behavior of composites. The increase in ac conductivity suggests that the oxygen vacancies (V''_O) (i.e., structural defects) are increased as the dopant concentration increases. Thus, as the structural defects increase, more will be oxygen vacancies, leading to an increase in ac conductivity. The E_a values show that these dielectric relaxation processes are related to V''_O. According to Ming-Ding et al. [51], the E_a of ABO_3 perovskite structures increases with a decrease in the oxygen vacancy. Therefore, conductivity may increase due to the charge carrier hopping rate or the oxygen vacancies (V''_O) (*i.e.*, structural defects) with temperature rise.

4 Conclusions

Lead-free composites of $1-x(K_{0.4}Na_{0.6}Nb_{0.96}Sb_{0.04}O_3)$-$x(Bi_{0.5}K_{0.5}TiO_3)$, $0.00 \le x \le$ x 0.07 were successfully prepared via a modified solid-state reaction route. Rietveld's refinement of the XRD patterns confirm the structural change from orthorhombic–rhombohedral–tetragonal with an increase in BKT content. In dielectric spectra, Curie temperature (T_C) shifted toward the room temperature with a rise in the BKT content. Dielectric relaxation was of the non-Debye type in all composites. The ac conductivity study confirms the NTCR behavior of the samples, and the increase in conductivity may be due to the oxygen vacancies or structural defects or due to the hopping mechanism. Therefore, these composites are suitable for energy storage device applications based on the above-discussed properties.

5 Prime nobility

Lead-free ceramics of $1-x(K_{0.4}Na_{0.6}Nb_{0.96}Sb_{0.04}O_3)$-$x(Bi_{0.5}K_{0.5}TiO_3)$ (where $0.00 \le x \le 0.07$) were prepared by a modified solid-state reaction route. Rietveld's refined XRD pattern revealed phase transitions from orthorhombic (Amm2)–rhombohedral (R3m) and rhombohedral to tetragonal (P4mm) with an increase in the content of $(Bi_{0.5}K_{0.5}TiO_3)$. A shift in T_C (Curie temperature) toward the room and below room temperature was observed with the addition of BKT content. The ac conductivity study confirms the NTCR behavior of the samples, and the increase in conductivity may be due to the oxygen vacancies/hopping mechanism or structural defects.

Acknowledgements

The author Madan Lal would like to thank Dr. Radheshyam Rai for his suggestions and help to carry out this work.

Author contributions

ML contributed to methodology, writing-original draft, conceptualization, data curation, supervision, and writing-review & editing. PT contributed to software and visualization. PT contributed to validation. NS contributed to resources. PS contributed to writing-review & editing. AKS contributed to validation.

Funding

The authors have not disclosed any funding.

Data availability

The data of this study will be made available from the corresponding author upon reasonable request.

Declarations

Conflict of interest The authors declare that they have no known competing financial interests or personal relationships that could have appeared to influence the work reported in this paper.

References

1. A. Kumar, S. Kumari, V. Kumar, P. Kumar, V.N. Thakur, A. Kumar, P. Goyal, A. Arya, A.L. Sharma, Synthesis, phase confirmation and electrical properties of (1–x) KNNS−xBNZSH lead-free ceramics. J. Mater. Sci. **33**(9), 6240–6252 (2022)
2. L. Tan, X. Wang, W. Zhu, A. Li, Y. Wang, Excellent piezoelectric performance of KNNS-based lead-free piezoelectric ceramics through powder pretreatment by hydrothermal method. J. Alloys Compd. **874**, 159770 (2021)
3. Y. Zhang, S. Wang, C. Chen, N. Zhang, A. Wang, Y. Zhu, F. Cai, Reduced hysteresis of KNNS-BNKZ piezoelectric ceramics through the control of sintering temperature. Ceram. Int. **44**(11), 12435–12441 (2018)
4. Y. Zhang, S. Wang, C. Chen, N. Zhang, A. Wang, Y. Zhu, F. Cai, Enhanced linearity of KNNS-BNKZ ceramics by combining the controls of phase composition and microstructure. Ceram. Int. **44**(7), 8380–8386 (2018)
5. P.J. Wang, D. Zhou, J. Li, L.-X. Pang, W.-F. Liu, J.-Z. Su, C. Singh, S. Trukhanov, A. Trukhanov, Significantly enhanced electrostatic energy storage performance of P (VDF-HFP)/ $BaTiO_3$-Bi $(Li_{0.5}Nb_{0.5})O_3$ nanocomposites. Nano Energy **78**, 105247 (2020)
6. X. Zhou, Z. Jia, A. Feng, X. Wang, J. Liu, M. Zhang, H. Cao, G. Wu, Synthesis of fish skin-derived 3D carbon foams with broadened bandwidth and excellent electromagnetic wave absorption performance. Carbon **152**, 827–836 (2019)
7. Y. Saito, H. Takao, T. Tani, T. Nonoyama, K. Takatori, T. Homma, T. Nagaya, M.J. Nakamura, Lead-free piezoceramics. Nature **432**(7013), 84–87 (2004)
8. S. Trukhanov, A. Trukhanov, M. Salem, E. Trukhanova, L. Panina, V. Kostishyn, M. Darwish, A.V. Trukhanov, T. Zubar, D.J. Tishkevich, Preparation and investigation of structure, magnetic and dielectric properties of $(BaFe_{11.9}Al_{0.1}O_{19})$ 1-x-$(BaTiO_3)$ x bicomponent ceramics. Ceram. Int. **44**(17), 21295–21302 (2018)
9. W. Peng-Jian, Z. Di, G. Huan-Huan, L. Wen-Feng, Ultrahigh enhancement rate of energy density of flexible polymer nanocomposites by core-shell $BaTiO_3$@ MgO structures as fillers. J. Mater. Chem. A **8**(22), 11124–11132 (2020)
10. M. Salem, L. Panina, E. Trukhanova, M. Darwish, A. Morchenko, T. Zubar, S. Trukhanov, A. Trukhanov, Structural, electric and magnetic properties of $(BaFe_{11.9}Al_{0.1}O_{1.9})$ 1-x-$(BaTiO_3)$ x composites. Composites Part B **174**, 107054 (2019)
11. D.V. Karpinsky, M.V. Silibin, S.V. Trukhanov, A.V. Trukhanov, A.L. Zhaludkevich, S.I. Latushka, D.V. Zhaludkevich, V.A. Khomchenko, D.O. Alikin, A.S.J.N. Abramov, Peculiarities of the crystal structure evolution of $BiFeO_3$–$BaTiO_3$ ceramics across structural phase transitions. Nanomaterials **10**(4), 801 (2020)
12. S. Jabarov, A. Mammadov, A.V. Trukhanov, Structural phase transition in $BaTiO_3$ at a constant volume under conditions of thermobaric effects. J. Surf. Investig. **11**, 223–225 (2017)
13. P. Li, J. Zhai, B. Shen, S. Zhang, X. Li, F. Zhu, X. Zhang, Ultrahigh piezoelectric properties in textured (K, Na) NbO_3-based lead-free ceramics. Adv. Mater. **30**(8), 1705171 (2018)
14. Y.-M. Li, Z.-Y. Shen, Y.-J. Liu, W.-C. Shen, Z.-M. Wang, High piezoelectric response in KNNS–xBNKZ lead-free ceramics. J. Mater. Sci. **26**(12), 9817–9820 (2015)
15. Y. Lin, J. Zhang, H. Yang, T. Wang, Excellent piezoelectric and magnetoelectric properties of the $(K_{0.45}Na_{0.55})$ 0.98 $Li_{0.02}$ $(Nb_{0.77}Ta_{0.18}Sb_{0.05})$ $O_3/Ni_{0.37}Cu_{0.20}Zn_{0.43}Fe_{1.92}O_{3.88}$ laminated composites. J. Alloys Compd **692**, 86–94 (2017)
16. M. Lal, M. Chandrasekhar, R. Rai, P. Kumar, Structural, dielectric and impedance studies of KNNS–BKT ceramics. Am. J. Mater. Sci. **7**(2), 25–34 (2017)
17. L. Su, K. Zhu, L. Bai, J. Qiu, H. Ji, Effects of Sb-doping on the formation of (K, Na)(Nb, Sb) O_3 solid solution under hydrothermal conditions. J. Alloys Compd. **493**(1–2), 186–191 (2010)
18. J. Wu, J. Xiao, T. Zheng, X. Wang, X. Cheng, B. Zhang, D. Xiao, J. Zhu, Giant piezoelectricity of (K, Na)(Nb, Sb) O_3–(Bi, Na, K, Pb) ZrO_3 ceramics with rhombohedral–tetragonal (RT) phase boundary. Scripta Mater. **88**, 41–44 (2014)

19. V. Ivanova, A. Kapyshev, Y.N. Venevtsev, G. Zhdanov, X-ray determination of the symmetry of elementary cells of the ferroelectric materials $(K_{0.5}Bi_{0.5})$ TiO_3 and $(Na_{0.5}Bi_{0.5})$ TiO_3 and of high-temperature phase transitions in $(K_{0.5}Bi_{0.5})$ TiO_3. Izv. Akad. Nauk SSSR **26**, 354–356 (1962)
20. J. Kim, Y. Sung, J. Cho, T. Song, M. Kim, H. Chong, T. Park, D. Do, S. Kim, Piezoelectric and dielectric properties of lead-free $(1–x)(Bi_{0.5}K_{0.5})$ $TiO_{3\text{-}x}$ $BiFeO_3$ ceramics. Ferroelectrics **404**(1), 88–92 (2010)
21. V. Isupov, $Na_{0.5}Bi_{0.5}TiO_3$ and $K_{0.5}Bi_{0.5}TiO_3$ perovskites and their solid solutions. Ferroelectric **315**(1), 123–147 (2005)
22. E.D. Pinheiro, T. Deivarajan, Influence of porous configuration on dielectric and piezoelectric properties of KNN–BKT lead-free ceramic. Appl. Phys. A **125**(11), 1–8 (2019)
23. P. Panda, B. Sahoo, PZT to lead free piezo ceramics: a review. Ferroelectrics **474**(1), 128–143 (2015)
24. H. Xing, P. Huang, C. Zhang, D. Li, Y. Zhang, W. Guo, G. Zhao, Q. Liao, Two new high Curie temperature piezoelectric ceramics. Mater. Lett. **160**, 38–40 (2015)
25. F. Li, Z. Tan, J. Xing, L. Jiang, B. Wu, J. Wu, D. Xiao, J. Zhu, Investigation of new lead free (1–x) KNNS–xBKZH piezoceramics with R-O–T phase boundary. J. Mater. Sci. **28**(12), 8803–8809 (2017)
26. B. Yan, H. Fan, A.K. Yadav, C. Wang, X. Zheng, H. Wang, W. Wang, W. Dong, S. Wang, Enhanced energy-storage performance and thermally stable permittivity for $K_{0.5}Na_{0.5}$-NbO_3 modified $[(Na_{0.5}Bi_{0.5})_{0.84}$ $Sr_{0.16}]$ 0.98 $La_{0.01}TiO_3$ lead-free perovskite ceramics. Ceram. Int. **46**(7), 9637–9645 (2020)
27. Z. Liu, H. Fan, S. Lei, X. Ren, C. Long, Duplex structure in $K_{0.5}Na_{0.5}NbO_3$-$SrZrO_3$ ceramics with temperature-stable dielectric properties. J. Eur. Ceram. Soc. **37**(1), 115–122 (2017)
28. M. Zou, H. Fan, L. Chen, W. Yang, Microstructure and electrical properties of $(1–x)[0.82$ $Bi_{0.5}Na_{0.5}TiO_3–_{0.18}$ $Bi_{0.5}$-$K_{0.5}TiO_3]–xBiFeO_3$ lead-free piezoelectric ceramics. J. Alloys Compd. **495**(1), 280–283 (2010)
29. J. Tangsritrakul, C. Tang, S. Day, D. Hall, Thermally-induced phase transformations in KNNS-BNKZ lead-free piezoceramics. J. Eur. Ceram. Soc. **40**(3), 672–681 (2020)
30. C. Long, T. Li, H. Fan, Y. Wu, L. Zhou, Y. Li, L. Xiao, Y. Li, Li-substituted $K_{0.5}Na_{0.5}NbO_3$-based piezoelectric ceramics: crystal structures and the effect of atmosphere on electrical properties. J. Alloys Compd. **658**, 839–847 (2016)
31. Q. Gou, J. Zhu, J. Wu, F. Li, L. Jiang, D. Xiao, Microstructure and electrical properties of (1–x) $K_{0.5}Na_{0.5}NbO_3–xBi_{0.5}$-$Na_{0.5}Zr_{0.85}Sn_{0.15}O_3$ lead-free ceramics. J. Alloys Compd. **730**, 311–317 (2018)
32. H. Wang, H. Yuan, Q. Hu, K. Wu, Q. Zheng, D. Lin, Exploring the high-performance (1–x) $BaTiO_3$-$xCaZrO_3$ piezoceramics with multiphase coexistence (ROT) from internal lattice distortion and domain features. J. Alloys Compd. **853**, 157167 (2021)
33. Y. Yang, H. Wang, Y. Li, Q. Zheng, J. Liao, W. Jie, D. Lin, Phase coexistence induced strong piezoelectricity in $K_{0.5}$ $Na_{0.5}$ NbO_3-based lead-free ceramics. Dalton Trans. **48**(28), 10676–10682 (2019)
34. H. Wang, Q. Hu, X. Liu, Q. Zheng, N. Jiang, Y. Yang, K. Kwok, C. Xu, D. Lin, A high-tolerance BNT-based ceramic with excellent energy storage properties and fatigue/frequency/thermal stability. Ceram. Int. **45**(17), 23233–23240 (2019)
35. H. Tao, J. Wu, Giant piezoelectric effect and high strain response in $(1–x)(K_{0.45}Na_{0.55})(Nb_{1-y}Sb_y)O_3$-$xBi_{0.5}Na_{0.5}$-$Zr_{1-z}HfzO_3$ lead-free ceramics. J. Eur. Ceram. Soc. **36**(7), 1605–1612 (2016)
36. X. Wang, J. Wu, X. Cheng, B. Zhang, J. Zhu, D. Xiao, Compositional dependence of phase structure and electrical properties in $(K_{0.50}Na_{0.50})0.97$ $Bi_{0.01}$ $(Nb_{1-x}Zr_x)$ O_3 lead-free ceramics. Ceram. Int. **39**(7), 8021–8024 (2013)
37. H. Wu, G. Wu, L.J.P.T. Wang, Peculiar porous α-Fe_2O_3, γ-Fe_2O_3 and Fe3O4 nanospheres: facile synthesis and electromagnetic properties. Power Technology **269**, 443–451 (2015)
38. K. Chen, J. Ma, C. Shi, W. Wu, B.J. Wu, Enhanced temperature stability in high piezoelectric performance of (K, Na) NbO_3-based lead-free ceramics trough co-doped antimony and tantalum. J. Alloys Compd. **852**, 156865 (2021)
39. D. Xue, Y. Liu, M. Shi, P. Wang, L. Zhang, G. Liu, Z. Chen, Y.J. Chen, Composition dependence of phase structure and piezoelectric properties in $(0.98–x)(K_{0.4}Na_{0.6})$ NbO_3–0.02 $CaZrO_{3}–_xBi_{0.5}$ $Na_{0.5}$ HfO_3 ternary ceramics. J. Mater. Sci. **29**, 2072–2079 (2018)
40. R. Mahbub, T. Fakhrul, M.F. Islam, Enhanced dielectric properties of tantalum oxide doped barium titanate based ceramic materials. Procedia Eng. **56**, 760–765 (2013)
41. Y. Chen, Y. Liu, D. Xue, Z. Xu, G. Liu, X. Liu, Z. Chen, X. Jiang, Effects of $BaHfO_3$ addition on the phase transition and piezoelectric properties of (K, Na) NbO_3-based ceramics. J. Alloys Compd. **735**, 68–74 (2018)
42. Y. Chen, D. Xue, P. Wang, X. Jiang, Z. Chen, X. Liu, G. Liu, Z. Xu, Lead-free $K_{0.5}$ $Na_{0.5}$ $NbO_3–Bi_{0.5}$ $Li_{0.5}$ $ZrO_3–BiAlO_3$ ternary ceramics: structure and piezoelectric properties. J. Electroceram. **40**(1), 36–41 (2018)
43. Y. Pan, X. Dai, J. Li, Y. Yi, Y. Yu, C. He, Y. Liu, Y. Xiang, Y. Chen, Multiphase coexistence and enhanced piezoelectric properties in $(1-x)(K_{0.45}Na_{0.55})(Nb_{0.965}Sb_{0.035})$ $O3-xBi_{0.5}$ $(K_{0.91}Li_{0.09})_{0.5}$ $(Hf_{0.3}Zr_{0.7})$ O3 lead-free ceramics. Physica Scripta **95**(6), 065802 (2020)
44. Y. Liu, Y. Yi, Y. Yu, Y. Pan, C. He, X. Liu, Z. Xu, G. Liu, Y. Chen, Microstructures, phase evolution and electrical

properties of (1–x) $K_{0.40}Na_{0.60}Nb_{0.96}Sb_{0.04}O_3$-x$Bi_{0.5}K_{0.5}$-$HfO_3$ lead-free ceramics. Ceram. Int. **45**(5), 6328–6334 (2019)

45. R. Rai, R. Rani, S. Sharma, A.L. Kholkin, Influence of Li and La content on phase structures and electrical properties of $K_{0.5}Na_{0.5}NbO_3$ lead-free piezoelectric ceramics. J. Alloys Compds. **2018**(577), 575–580 (2013)
46. R. Zuo, J. Fu, D. Lv, Y. Liu, Antimony tuned rhombohedral-orthorhombic phase transition and enhanced piezoelectric properties in sodium potassium niobate. J. Am. Ceram. Soc. **93**(9), 2783–2787 (2010)
47. A. Singh, R. Chatterjee, Structural and electrical properties of BKT rich $Bi_{0.5}K_{0.5}TiO_3$-$K_{0.5}Na_{0.5}NbO_3$ system. AIP Adv. **3**(3), 032129 (2013)
48. M. Lal, M. Shandilya, R. Rai, A. Ranjan, S. Sharma, M. Valente, Study of structural, electrical and magnetic properties of 1–x ($Ba_{0.96}$ $Ca_{0.04}$ TiO_3)– x ($BiFeO_3$) ceramics composites. J. Mater. Sci. **29**(16), 13984–14002 (2018)
49. J. Joshi, D. Kanchan, M. Joshi, H. Jethva, K. Parikh, Dielectric relaxation, complex impedance and modulus spectroscopic studies of mix phase rod like cobalt sulfide nanoparticles. Mater. Res. Bull. **93**, 63–73 (2017)
50. A. Faisal, H. Sobhi, B.M. Lamjed, B. Michel, D. Abdessalem, Synthesis and study of impendence spectroscopy properties of $La_{0.6}$ $Ca_{0.2}$ $Na_{0.2}$ MnO_3 manganite perovskite prepared using sol–gel method. J. Mater. Sci. **31**(11), 8248–8257 (2020)
51. M.-D. Li, X.-G. Tang, S.-M. Zeng, Y.-P. Jiang, Q.-X. Liu, T.-F. Zhang, W.-H. Li, Oxygen-vacancy-related dielectric relaxation behaviours and impedance spectroscopy of Bi (Mg1/2Ti1/2) O_3 modified $BaTiO_3$ ferroelectric ceramics. J Mater. **4**(3), 194–201 (2018)